



# Computational modeling of an ion-driven nanomotor

A. Lohrasebi<sup>a,\*</sup>, H. Rafii-Tabar<sup>a,b</sup>

<sup>a</sup> Computational Physical Sciences Research Laboratory, Department of Nano-Science, Institute for Research in Fundamental Sciences (IPM), P.O. Box 19395- 5531, Tehran, Iran

<sup>b</sup> Department of Medical Physics and Biomedical Engineering, Shahid Beheshti University of Medical Sciences, Evin, Tehran, Iran

## ARTICLE INFO

### Article history:

Received 4 January 2008

Received in revised form 17 March 2008

Accepted 17 March 2008

Available online 27 March 2008

### Keywords:

Nanomotor

F<sub>0</sub>-like motor

Stochastic molecular dynamics

## ABSTRACT

The dynamics of an ion-driven rotary nanomotor, mimicking the F<sub>0</sub> part of the ATPase biomolecular motor, in the presence, and absence, of an external electric field have been simulated via the application of the stochastic molecular dynamics (MD) method. The rotary motion of the proposed motor arises as a result of an ion gradient established between the outer and inner parts of the environment within which the motor is embedded. We show that the operation of this motor can be controlled by such parameters as the amount of the positive ions placed in the stator part of the motor, the density of the positive ions, and the strength and frequency of the applied electric field.

© 2008 Elsevier Inc. All rights reserved.

## 1. Introduction

We propose a nano-scale rotary motor inspired by the F<sub>0</sub> part of ATPase protein-motor. The ATPase biomolecular motor synthesizes the adenosine three phosphate (ATP) molecules [1,2] that act as the biological fuel for the intracellular protein-motors, such as kinesins. The ATPase is composed of two main protein-motors, referred to as the F<sub>0</sub> and F<sub>1</sub> parts. The F<sub>0</sub> part is embedded in the mitochondrial membrane, and is powered by positive ions whose flow generates the rotary motion. The F<sub>1</sub> part is located outside the membrane and synthesizes the ATP molecules by employing the rotary motion of the F<sub>0</sub> part.

Our proposed nanomotor is constructed from single-walled carbon nanotubes (SWCNTs), together with benzene rings and graphene sheets. SWCNTs have been employed in the past to design nano-scale devices, such as nanomotors [3,4], gears [3,5], bearings [6] and oscillators [7]. Let us review, very briefly, some of the nanotube-based devices that have been designed in the past. The first such device, designed via the application of the MD simulation method, was a laser-driven nanomotor [5] composed of two concentric nanotubes, acting as a sleeve and a shaft. A pair of positive and negative electric charges were located on two carbon atoms of the end ring of the sleeve part. Applying one or two oscillating electric fields, induced a rotary motion in the sleeve part. The optimum range of the frequency depended on the size of the motor, and the relative positions of the attached charges. If the

frequency of the external field were not in that optimum range, the motor displayed a pendulum-like, rather than a rotary, motion.

Another MD study [4] was concerned with the design of a nanogear, composed of two SWCNTs that were covalently bonded to benzene rings, acting as the gear teeth. The gear was again driven by a laser electric field. To generate the rotary motion of the gear, positive and negative charges were located on the end of the gear. It was found that the frequency of the applied laser field must be set at near intrinsic frequency of the nanogear so as to induce rotation.

A third MD-based simulation investigated the stability of the mechanically driven nanogears [3], and it was shown that when one of the gears was put into motion by rotating the atoms near the end of its nanotube, the second nanotube began its rotation because of the meshing of the respective benzene rings that allowed the transfer of the angular momentum from the first gear to the second one. Furthermore, it was found that this system could operate in a stable mode if the gears rotated with a frequency under 100 GHz, with the temperature lower than 600 K.

A further MD-based simulation has investigated the construction of a nano-scale engine [8], composed of a SWCNT with and without attached benzene rings, rotated by a fluidic gas. The gas flow was produced by an oscillator in the form of a capped nanotube placed inside the larger nanotube acting as a sleeve. It was shown that, the flow rate, which could be controlled by the frequency of the oscillator, and the density of the fluid, were the crucial parameters in the operation of this motor. It was found that the motor whose nanotube was decorated with benzene rings was more efficient.

Recently, another MD-based simulation was performed [9], to investigate a charge-driven molecular water pump. In this

\* Corresponding author. Tel.: +98 2122835061; fax: +98 2122835058.  
E-mail address: [lohrasebi@nano.ipm.ac.ir](mailto:lohrasebi@nano.ipm.ac.ir) (A. Lohrasebi).

simulation, the nanopump was designed by mimicking the structure of channels in a cellular membrane that transport water in and out of the cell. The nanopump was composed of an uncapped armchair SWCNT located between two graphene sheets, with three positive charges positioned adjacent to the nanotube. It was shown that, the flow of the water in the nanotube was dependent on the spatial positions of the positive charges.

A further recent MD-based simulation study [10], considered a nanopropeller formed from a functionalised (8,0) SWCNT. The propeller can pump liquid along the axis of the nanotube when the two blades, made from pyrene molecules and attached to the opposite sides of the carbon nanotube and tilted with respect to its axis, are rotated mechanically. The simulation revealed that pumping depended significantly on the chemistry of the blade-liquid interface. The propeller was used both in hydrophobic and hydrophilic liquids, and it was shown that the pumping efficiency was very sensitive to the size, shape, chemical, or biological compositions of the nanoblades.

In this paper, we have employed both the standard version of the classical MD simulation method, and its stochastic variation [11], to simulate the dynamics of an  $F_0$ -like rotary nanomotor, composed of two SWCNTs located between a number of graphene

sheets, and powered by a positive-ion gradient. The motor can generate a rotary motion in such environments like the interior of a cell which contains  $\text{Na}^+$  ions.

## 2. Atomistic structure of the proposed nanomotor

The schematic structure of the proposed nanomotor is shown in Fig. 1. The nanomotor is composed of two main sections. The first section, referred to as the *rotor*, is made of two coaxial (10,10) and (18,18) SWCNTs of lengths 23 and 10 Å respectively. The inner nanotube is capped, and 20 benzene rings are used to couple the 2 nanotubes together, as shown in Fig. 1b. The rings divide the space between the two SWCNTs into 10 identical segments. A negative charge is located in each of the 10 segments, on the inner nanotube, giving a total charge of  $-10e$  on the rotor part.

The second section of the nanomotor is made of six graphene sheets, as shown in Fig. 1c, of the same area of  $39 \text{ Å} \times 37.5 \text{ Å}$  with central circular cavities and two small holes in the upper and lower graphene sheets, as shown in Fig. 1d. The rotor passes through the cavities. The radii of the holes in the upper and the lower graphene sheets are set at  $10.5 \text{ Å}$ , and for the rest of the holes are set at  $16 \text{ Å}$ . The radii of the two small holes in the upper and lower sheets are

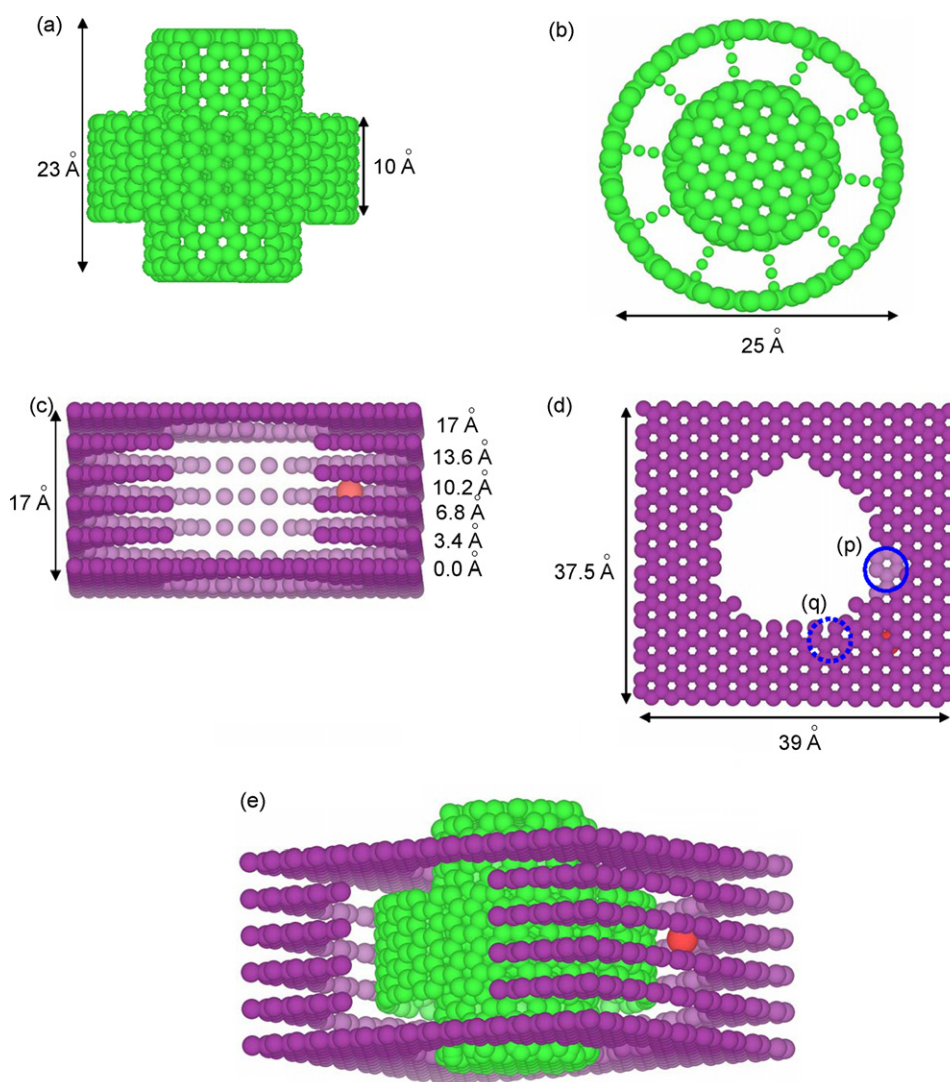


**Fig. 1.** The structure of nanomotor components: (a) side view of the rotor. The rotor is composed of 2 nanotubes and 20 benzene graphene rings that divide the rotor into 10 equal parts; (b) top view of the rotor; (c) three-dimensional view of the six graphene sheets; (d) top view of the six graphene sheets. The entrance and the exit holes are shown by solid (p) and dashed (q) circles; (e) complete structure of the nanomotor.

set at 4 Å and are centered on the perimeter of the upper and lower cavities. These small holes are used for ion transport, with one of them acting as the entrance channel, the other acting as the exit channel. Positive charges, with strength ranging from 1e to 5e, are attached to a carbon atom on the perimeter of the cavity in the third graphene sheet from the top, and located between the entrance and the exit channels. This is referred to as the *stator charge*, and is shown in Fig. 1e, which also shows the overall schematics of the proposed motor.

### 3. Computational details

#### 3.1. Inter-atomic and inter-ionic potentials

Three types of interatomic potential were used in the simulations. These were: the first generation Brenner potential [12] for modeling the covalent bonding between the carbon (C) atoms within the nanotubes, within the graphene sheets, and within the benzene rings; the Lennard–Jones (LJ) potential, describing the non-bonding interactions C–Na<sup>+</sup>, Na<sup>+</sup>–Na<sup>+</sup>, and the C–C interactions in the nanotube–graphene, and graphene–graphene systems. The parameters of the LJ potential were  $\epsilon_{\text{Na}^+} = 0.019044$  eV, and  $\sigma_{\text{Na}^+} = 4.1$  Å for the Na<sup>+</sup>–Na<sup>+</sup> interaction in water [13], and  $\epsilon_{\text{C}} = 0.002413$  eV and  $\sigma_{\text{C}} = 3.4$  Å for the C–C interaction [14]. The parameters for the C–Na<sup>+</sup> interaction were calculated by using the Lorentz–Berthelot mixing rules, i.e.  $\epsilon_{\text{Na}^+-\text{C}} = \sqrt{\epsilon_{\text{Na}^+} \times \epsilon_{\text{C}}}$ , and  $\sigma_{\text{Na}^+-\text{C}} = 0.5(\sigma_{\text{Na}^+} + \sigma_{\text{C}})$ .

The electrostatic interactions were modeled by the application of the Reaction Field (RF) method [15–17], wherein all charges located inside a spherical cavity of radius  $R_{\text{C}} = 14$  Å [17] interact via

$$U_{\text{elc}} = \frac{e_i e_j}{4\pi\epsilon_0 r_{ij}} + U_{\text{RF}}, \quad (1)$$

where  $r_{ij}$  is the distance between particles (sites)  $i$  and  $j$ , with charges  $e_i$  and  $e_j$ ,  $\epsilon_0$  the dielectric constant of the vacuum, and  $U_{\text{RF}}$  describes the interactions between charges located outside this sphere, and is given by

$$U_{\text{RF}} = \frac{e_i e_j (\epsilon_{\text{RF}} - 1) r_{ij}^2}{4\pi\epsilon_0 (2\epsilon_{\text{RF}} + 1) R_{\text{C}}^3}, \quad (2)$$

where  $\epsilon_{\text{RF}} = 87.7$  [17] is the dielectric constant of the continuum outside the cavity.

#### 3.2. Equations of motion

The dynamics of all carbon atoms were described by Newton's differential equation of motion, integrated via the application of the velocity Verlet method [11], with the integration time-step,  $dt = 0.6$  fs. This value of  $dt$  was arrived at after performing the simulations with several other values and observing that this value ensured the structural stability of the motor. Smaller values  $dt$  did not result in structural instability, but were computationally more expensive. The motion of Na<sup>+</sup> ions in the water environment, above and below the nanomotor, was modeled via the stochastic differential equation [18]

$$m \frac{d^2 r}{dt^2} = -\frac{dU}{dr} - \eta \frac{dr}{dt} + \Gamma_{\text{rand}}(t), \quad (3)$$

where the first term on the RHS represents the deterministic force obtained from the sum of the potentials  $U$ , i.e. the Brenner, the LJ and the  $U_{\text{elc}}$  potentials, the second term represents the drag force,

where  $\eta$  is the drag coefficient,

$$\eta = \frac{k_{\text{B}} T}{D}, \quad (4)$$

with  $D = 0.29 \times 10^{-9}$  (m<sup>2</sup>/s<sup>−1</sup>) [19] being the the diffusion coefficient of Na<sup>+</sup> in the water, and the third term represents the stochastic, or the Brownian, force due to the randomly fluctuating water medium.

The simulations were performed via our own FORTRAN-based code, considered a constant-NVT ensemble, with the temperature control implemented via the application of the Nosé–Hoover thermostat [20,21] in the velocity Verlet algorithm [22].

#### 3.3. System details

The total number of carbon atoms in our system was 2350, and number of Na<sup>+</sup> ions ranged between 50 and 250 depending on the simulation. The particles were confined in a rectangular simulation box with dimensions of  $L_x = 40$ ,  $L_y = 38.5$  and  $L_z = 117$  Å. The  $x$ - and  $y$ -dimensions of the simulation box were set at slightly larger values than those of the graphene sheets. This is a normal practice since the atoms cannot be treated as point particles, and therefore there is an ambiguity as to where the boundaries of the simulation box intersect the boundary atoms.

The total *net* amount of charge in the system, taking into account the negative charges in the rotor, varied between 40e and 245e. Periodic boundary conditions were applied in the  $x$ - and  $y$ -directions. The simulations were performed at temperatures  $T = 300$  and 500 K.

## 4. Results and discussion

#### 4.1. The overall simulation process

The system was equilibrated for 200 ps at a constant temperature without the presence of the ionic gradient, i.e. the nanomotor and the collection of the positive ions were equilibrated independently without any interactions between them. During equilibration, the total energy of the system was used as the parameter for monitoring whether system has reached the equilibrium state. When fluctuations in energy were compatible with the thermal fluctuations, the equilibration phase was terminated.

The ions entered the nanomotor via the entrance hole and left the nanomotor via the exit hole, transporting through the channel, constructed from the graphene sheets. The upper and lower sheets also acted as boundaries separating the main part of the nanomotor from the ion reservoirs. The overall operation of the motor was as follows. A positive ion entered the channel. It then sensed the positive stator charge, which, as was said above, could range between 1e and 5e, together with the rotor negative charge of −1e located on each of the 10 segments of the rotor part. It was then attracted to the negative charge on the rotor segment, and was repelled by the positive stator charge. This repulsive interaction induced a torque on the rotor, causing it to rotate. The rotation caused the next negative site on the rotor to face the next positive ion coming through the transport channel. When a complete anti-clockwise rotation of the rotor was performed, the positive ion was ready to leave the stator and exit the channel through the exit hole, and reach the space under the lower graphene sheet.

The first simulations were performed in the presence of an ion gradient. The ion gradient was established by setting the ion density in the upper section of the nanomotor at 5 M (molar), and

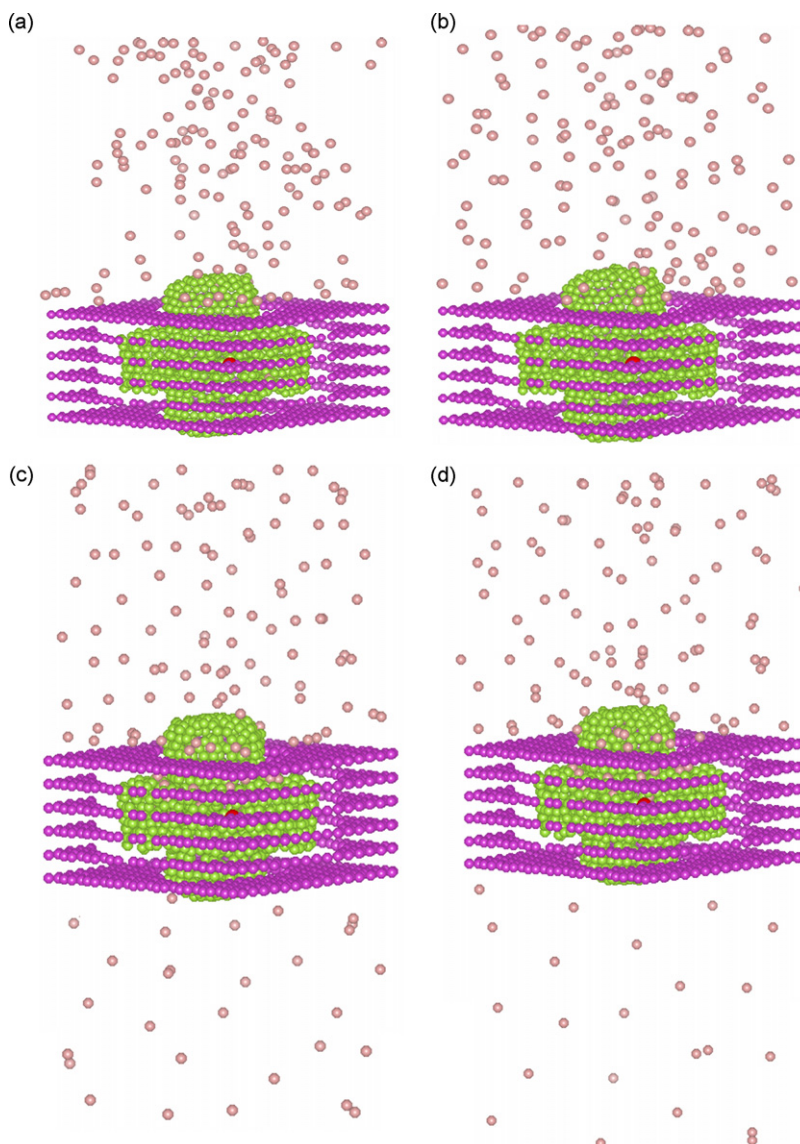


**Fig. 2.** The snapshots of the our overall simulation process: (a) and (b) after equilibration at  $T = 300$  and  $500$  K, respectively; (c) and (d) following equilibration after  $900$  ps at  $T = 300$  and  $500$  K, respectively. The ion density was set at  $5$  M. The ions enter the nanomotor from the high ion density side, and exit the motor through the lower graphene sheet.

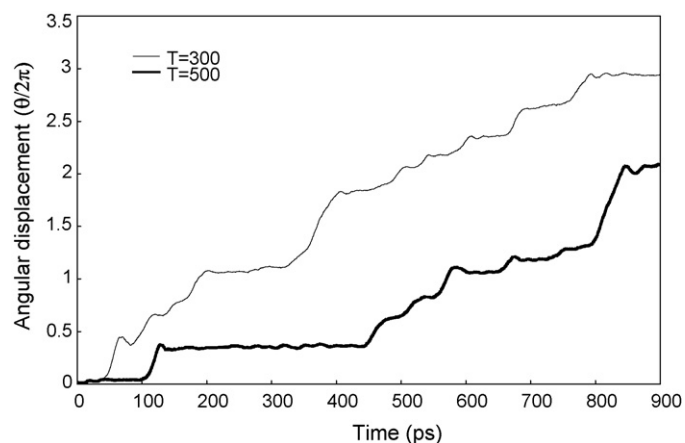


**Fig. 3.** Variation of rotational angle with simulation time at  $T = 300$  and  $500$  K. The stator charge was set at  $4e$ , and the ion density was set at  $5$  M.

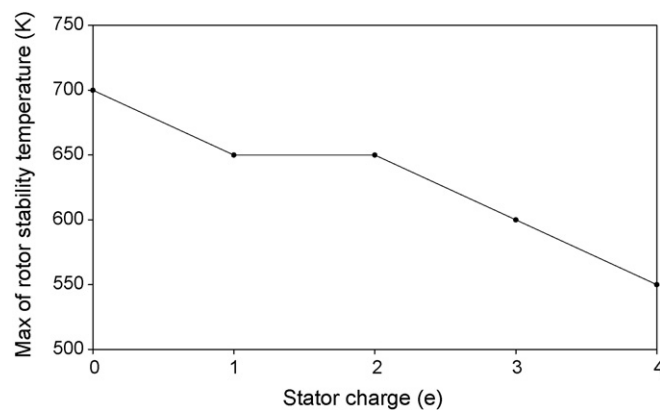


**Fig. 4.** Variation of temperature with the stator charge. When the stator charge is increased, the maximum temperature at which the nanomotor is stable is decreased.



at zero in the lower section of the nanomotor. The stator charge was set at  $4e$ , and the temperature was set at  $T = 300$  and  $500$  K.

Following the equilibration phase, the nanomotor was simulated for a period of 900 ps. The simulation snapshots corresponding to the state of the nanomotor at the equilibration, and at the conclusion of the simulation phase are shown in Fig. 2 for the above temperatures. Fig. 3 shows the variation of the rotational angle of the nanomotor with time during the entire course of simulation. As can be seen from this figure, the angular motion of the rotor at the lower temperature is higher than its motion at the higher temperature, since at the higher temperature there is a higher degree of thermal fluctuation, slowing down the angular motion of the nanomotor. The step-like feature observed in Fig. 3 shows that when an ion entered the nanomotor, it caused an increase in its rotational angle, while the flat regions on the graph correspond to the situations whereby the nanomotor was awaiting for the arrival of an ion. We found that the time-average values of the rotational frequency of rotor were 3 and 2.2 GHz for  $T = 300$  and  $500$  K, respectively.

#### 4.2. Influence of temperature on the stability of nanomotor

Our aim here was to analyse the dependence of the structural stability of the nanomotor on temperature. This was done for various amount of the stator charge, in order to find out the maximum temperature for which the nanomotor did not structurally collapse, i.e. its geometric shape was preserved. This part of the MD simulation was performed without the presence of an ion gradient. Fig. 4 shows this variation, and it can be seen from this figure that when the stator charge increases, the maximum temperature decreases. This behavior is displayed because when the temperature is increased, the bonds between the carbon atoms weaken, and since the attractive force is increased due to an increase in the stator charge, then the weakening of the bonds on the one hand, and the increase in the attractive force on the carbon atoms on the other hand, give rise to the appearance of structural instability and the eventual collapse of the nanomotor. For example, when the stator charge was set at  $4e$ , the nanomotor could work under  $T = 550$  K, as can be observed from Fig. 4.

#### 4.3. Influence of the stator charge and ion density on the nanomotor frequency

To ascertain the influence of the amount of the stator charge on the frequency of the nanomotor, for a fixed temperature, the MD simulation was performed in the presence of an ion gradient at the above two temperatures. The system was equilibrated, and simulated, in the manner described above. Fig. 5a shows the variation of the rotational frequency of the nanomotor with the stator charge for the two temperatures. It is seen that when the stator charge increases, the frequency also increases, up to a point, i.e. the rotation rate of rotor is increased, since by increasing the charge on the stator, the induced torque on the rotor is increased. This behavior is seen for both temperatures. However, when the amount of the stator charge reaches  $5e$ , the frequency of the nanomotor begins to decline and eventually reaches zero. This behavior is due to the fact that when the stator charge is increased to  $5e$ , the electrostatic force between the negative sub-unit of the rotor and the stator charge becomes very large and promotes a structural collapse of the nanomotor, as seen in the simulation snapshots shown in Fig. 6.

Next, we examined the role of the *location* of the stator charge on the rotational frequency of the nanomotor. In the MD simulation, the location of the stator charge was varied in two ways, either it was moved from one graphene sheet to another

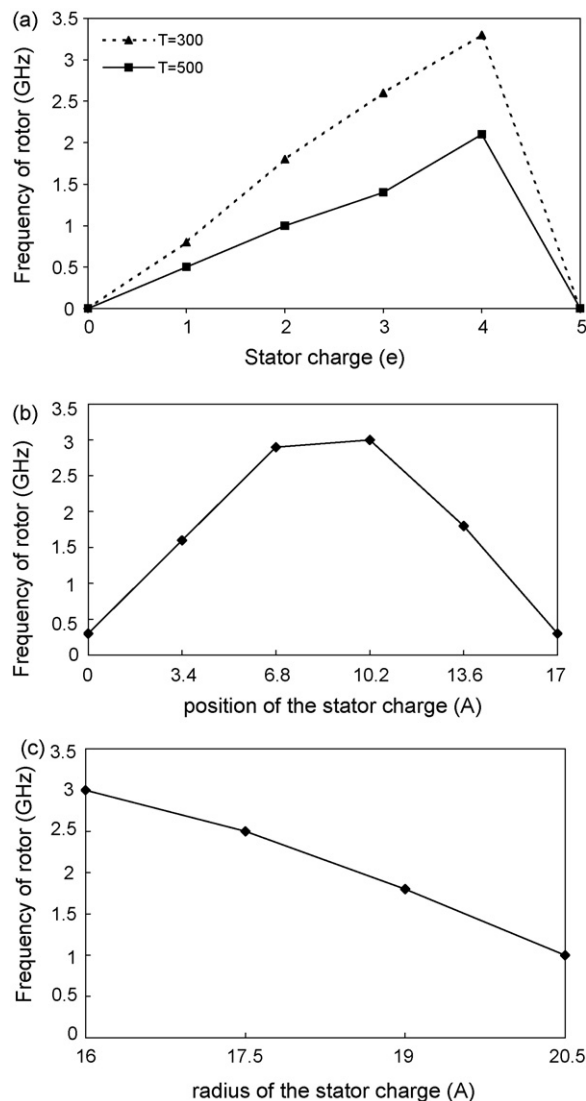


**Fig. 5.** (a) Variation of rotor frequency with the stator charge at  $T = 300$  and  $500$  K. The ion density was set at  $5$  M in the upper part of the nanomotor; (b) variation of rotor frequency with the  $z$  location of the stator charge. The  $z$  distance is measured from the bottom graphene sheet. The simulation temperature was set at  $300$  K and the stator charge was set at  $4e$ ; (c) variation of the rotor frequency with radial position of the stator charge measured from the rotor axis. The temperature was set at  $300$  K, the stator charge was set at  $4e$ , and the ion density was set at  $5$  M.

(case I), i.e. it was moved vertically, or it was moved horizontally on a particular graphene sheet (case II) away from the axis of the rotor. Fig. 5b shows the variation of the rotational frequency with the location of the stator charge for case I for  $T = 300$  K. The amount of the stator charge was set at  $4e$ , and the ion gradient, and the length of the equilibration and the simulation phases, were the same as those stated above. From this figure, it can be seen that when the charge is positioned on the same graphene sheet that contains the entrance hole, or the exit hole, the rotational frequency is decreased. The distance of the charge from these holes was set at  $4$  Å from the edge of the holes. It should be remarked that when the charge was positioned on the upper, or lower, sheet, its  $x$  and  $y$  positions were the same as the  $x$  and  $y$  positions before it was moved, i.e.  $x = y = 11.5$  Å. Only the  $z$ , or the vertical, coordinate of the charge was changed.

This behavior can be explained, by observing that when the stator charge is located on either the upper, or the lower, graphene sheet, it acts as a potential barrier for the ions entering, or exiting

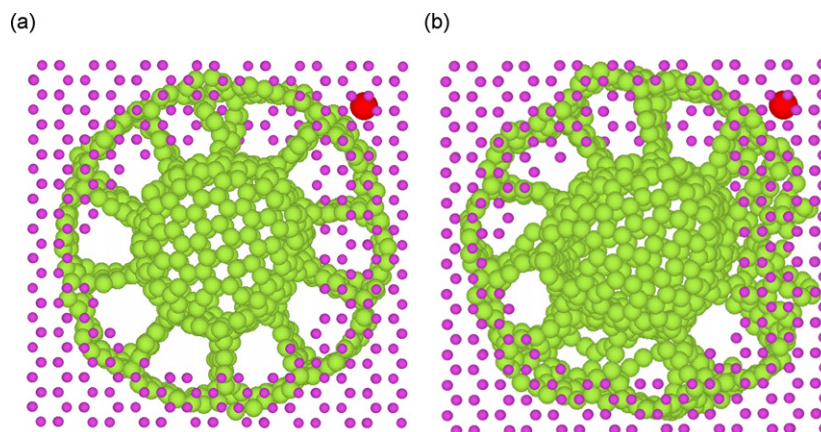


Fig. 6. Simulation snapshots, at  $T = 300$  K, of the rotor part after equilibration for two different stator charge: (a) 4e and (b) 6e.

the transport channels, hence, because a fewer number of ions are allowed to enter the channel, the motor frequency is correspondingly reduced.

Fig. 5c shows the same variation for case II. Here, we observe that as the location of the stator charge is moved away from the axis of the rotor, the rotational frequency is decreased. This behaviour arises because when the charge is moved away from the axis, the electrostatic-induced torque is reduced as a result of an increase in the distance between the stator and rotor charges.

Finally, the influence of the variation of the ion density, present on the upper part of the nanomotor, with the rotational frequency was examined. The temperature was set at  $T = 300$  and  $500$  K, and the stator charge was set at 4e. The equilibration and the simulation periods were the same as those stated above. Fig. 7 shows this variation. As is evident from this figure, we have used an ion density in the range 1–5 M. Going back to Fig. 2, we see that a density of 5 M led to the transport of 30 ions through the nanomotor in 900 ps, i.e. to the transport of  $3 \times 10^{10}$  ions per second. The ion transport in a biological nanomotor (BNM) is approximately  $10^8$  ions per second, while that of the ATPase motor is approximately  $2 \times 10^3$  [1]. Comparison of these two values shows that the ion transport rate in our proposed nanomotor was some 300 times greater than that in a BNM. This higher value can be explained on several grounds. Firstly, our nanomotor is much lighter in weight than the BNM, hence more rotations are performed by the rotor in our proposed nanomotor than in a BNM, leading to the exit of a greater number of ions. Secondly, in a BNM, the ion gradient corresponds to outer and inner ionic

densities of, respectively, 350 and 50 mM [1]. These density values are far smaller than those used in our computations. Had these density values been used in our MD simulations, no ions would have transported through the channel during any reasonable computational time. For instance, it would have taken 10 ns for one ion to go through the transport channel. Therefore, our choice of the ion transport rate was dictated, to a large extent, by computational constraints.

Coming back to Fig. 7, it can be observed that as the ion density increases, the frequency of the nanomotor increases, since there is more chance for the ions to enter the transport channel.

#### 4.4. Influence of the external electric field on the frequency of the nanomotor

We have also investigated the influence of an external electric field on the performance of the nanomotor. The influence of both the intensity and the frequency of the applied field were investigated. The applied electric field had the form  $E_0 \cos(\omega t)$ , wherein  $E_0$  and  $\omega$  are, respectively, the amplitude and the frequency of external field, and  $t$  is the simulation time. In these simulations, the stator charge was at 4e, and the ion density was set at 5 M. The equilibration and the simulation periods were the same as before. The electric field direction was normal to axis of the nanomotor.

Fig. 8a shows the variation of the field frequency with the rotational frequency of the nanomotor. These results were obtained for a fixed field amplitude of  $E_0 = 2.5$  MV/m, and a field frequency in the range  $10^9$ – $10^{15}$ . This value of  $E_0$  was found to be the minimum value that could be chosen so that the external field could show its effect on the performance of the nanomotor. It was found that any value smaller than this would have led to a negligible influence of the field on the frequency. This frequency range was chosen because any smaller value than the lower limit would have prevented a change of direction of the field during the simulation time, i.e. the field would have acted as a dc field. For example, if the frequency were set at  $10^8$ , the corresponding time to induce a change of direction would have been  $5 \times 10^{-9}$  s, while our simulation period was 900 ps. Hence, during this simulation time period, no change of direction would have been observed. It should, however, be remarked that if the simulation time period were increased, we could have used smaller values of the field frequency, and also observe their effects. Hence, our choice of the frequency range was dictated purely by computational convenience.

From Fig. 8a, we observe that as the frequency of the applied field increases, the rate of increase in the frequency of the

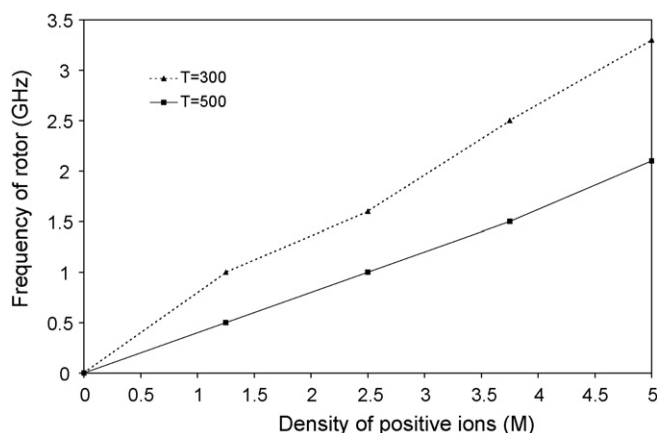
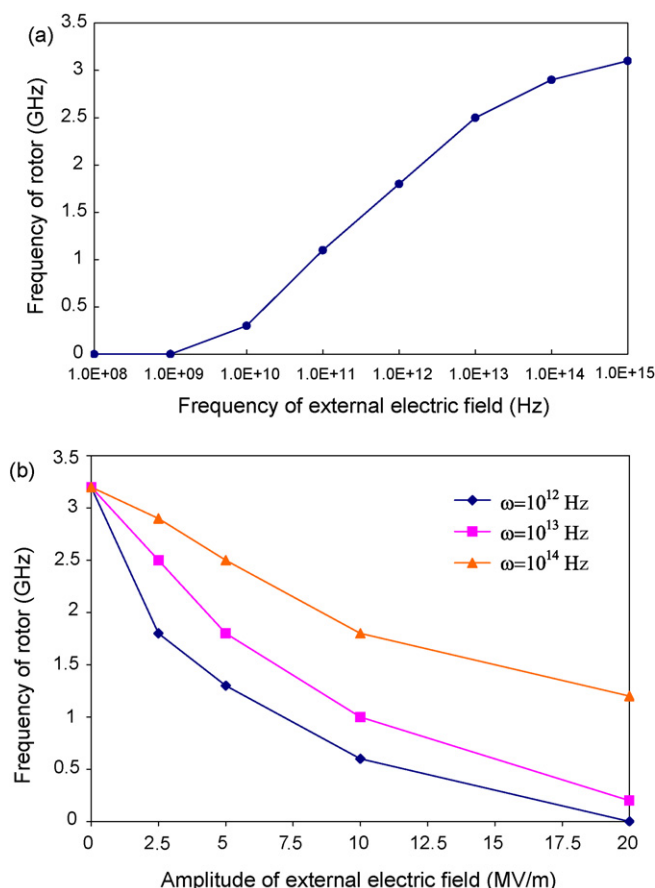


Fig. 7. Variation of the rotational frequency with the ion density at  $T = 300$  and  $500$  K, for the stator charge of 4e.



**Fig. 8.** (a) Variation of rotational frequency with the frequency of the external electric field for fixed amplitude of  $E_0 = 2.5$  MV/m; (b) variation of rotational frequency with the amplitude of the external electric field for three different field frequencies, at  $T = 300$  K, and the stator charge was set at  $4e$  and the ion density was set at  $5$  M.

nanomotor slows down, and the variation tends towards a constant value, i.e. at higher frequencies of the applied field, the nanomotor rotates with a constant frequency.

Fig. 8b shows the variation of the nanomotor frequency with the amplitude  $E_0$  of the applied field, in the range  $2.5$ – $20$  MV/m, for three field frequencies  $\omega = 10^{12}$ ,  $10^{13}$  and  $10^{14}$  Hz. It is seen that as the amplitude increases, the rotational frequency decreases. This behavior can be explained by noticing that as the amplitude is increased, the force experienced by the ions is also increased, and since this force is along the direction perpendicular to the direction of motion of ions entering the channel, hence fewer number of ions can enter the channel, and consequently the rotational frequency is decreased.

## 5. Conclusions

In this paper, we have provided the outline of an ion-driven nano-scale motor, mimicking to a large extent the mechanism underlying the rotary motion of the  $F_0$  part of an  $F_0F_1$  ATPase bionanomotor. Deterministic and stochastic MD simulations, based on many-body, and two-body, interatomic potentials, were employed to model the dynamics of such a nanomotor and to examine the influence of environmental parameters, such as temperature, on this dynamics. The temperature range considered included values that are met in a biological system. Furthermore, we have also examined the influence of an external electric field on the behavior of this nanomotor. This part of research can open the

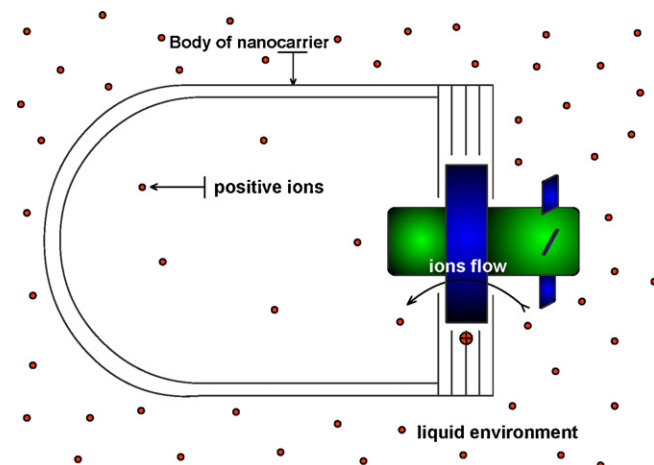


**Fig. 9.** Schematic representation of a proposed nanocarrier, made from capped double-walled carbon nanotubes, and consisting of four nanoblades covalently attached to the rotor part, and acting as propeller.

prospect of examining the influence of electromagnetic fields on biological tissues, for instance to see how an RF radiation affects the behaviour of biomembranes and bionanomotors. We have found that, as far as the temperature is concerned, the proposed nanomotor is structurally stable below  $T = 550$  K, i.e. for temperatures above this value, the nanomotor can structurally disintegrate.

We have also found that the application of an external field can lead to a reduction in the rotational frequency of the nanomotor by influencing the rate of transport of ions into the channel of the nanomotor. Furthermore, our simulations show that we can use the amount of charge on the stator, its spatial location, and the ion gradient as parameters to exercise control over the working of such a motor.

In this paper, we have provided a computational model of a generic nanomotor that could operate in a rather complex environment. Our aim was not to provide a model for a specific device which would perform a specific task. The proposed nanomotor could be used, for instance, as part of a nanocarrier, shown schematically in Fig. 9. Such a carrier could move in a complex charged-liquid environment containing, for instance, positive ions. Such an environment could represent the interior of a biological cell. The carrier could be made from capped double-walled carbon nanotubes. Four nanoblades could be covalently attached to the rotor part of the nanomotor, acting as blades [10]. The way such a nanocarrier works is that as the positive ions move to the interior of the carrier, they induce a rotational motion, propelling the container forward. The speed of motion can be controlled by using the parameters discussed above, such as the amount, or the spatial location, of the stator charge. When there is no longer an ion gradient operating, the nanocarrier ceases its motion. Therefore, such a carrier could operate for a specific period of time, delivering cargoes, such as drugs, to specific locations.

## Acknowledgment

We would like to thank A. Vaez for his contributing to writing the potential part of the code.

## References

- [1] J. Xing, H. Wang, C.V. Ballmoos, P. Dimroth, G. Oster, Torque generation by the  $F_0$  motor of the sodium ATPase, *Biophys. J.* 87 (2004) 2148–2163.
- [2] G. Oster, H. Wang, Reverse engineering a protein: the mechanochemistry of ATP synthase, *Biochem. Biophys. Acta* 1458 (2000) 482–510.

- [3] J. Han, A. Globus, R. Jaffe, G. Deardorff, Molecular dynamics simulation of carbon nanotube-based gears, *Nanotechnology* 8 (1997) 95.
- [4] R.E. Tuzun, D.W. Noid, B.G. Sumpter, Dynamics of a laser driven molecular motor, *Nanotechnology* 6 (1995) 52.
- [4] D.A. Srivastava, Phenomenological model of the rotation dynamics of carbon nanotube gears with laser electric fields, *Nanotechnology* 8 (1997) 186.
- [6] S. Zhang, W.K. Liu, R.S. Ruoff, Atomistic simulations of double-walled carbon nanotubes as rotational bearings, *Nanoletters* 4 (2004) 293.
- [7] J.W. Kang, K.O. Song, O.K. Kwon, H.J. Hwang, Carbon nanotube oscillator operated by thermal expansion of encapsulated gases, *Nanotechnology* 16 (2005) 2670–2676.
- [8] J.W. Kang, H.J. Hwang, Nanoscale carbon nanotube motor schematics simulations for micro-electro-mechanical machines, *Nanotechnology* 15 (2004) 1633–1638.
- [9] X. Gong, J. Li, H. Lu, R. Wan, J. Li, J. Hu, H. Fang, A charge-driven molecular water pump, *Nature* 2 (2007) 709–712.
- [10] B. Wang, P. Kral, Chemically tunable nanoscale propellers of liquids, *Phys. Rev. Lett.* 98 (2007) 266102.
- [11] M.P. Allen, D.J. Tildesley, *Computer Simulation of Liquids*, Clarendon, Oxford, 1987.
- [12] D.W. Brenner, Phys. Empirical potential for hydrocarbons for use in simulating the chemical vapor deposition of diamond films, *Phys. Rev. B* 42 (1990) 9458.
- [13] P.S. Crozier, D. Henderson, R.L. Rowley, D.D. Busath, Model channel ion currents in NaCl-SPC/E solution with applied-field molecular dynamics, *Biophys. J.* 81 (2001) 3077–3089.
- [14] G. Stan, M.J. Bojan, S. Curtarolo, S.M. Gatica, M.W. Cole, Uptake of gases in bundles of carbon nanotubes, *Phys. Rev. B* 62 (2000) 2173.
- [15] M. Neumann, The dielectric constant of water. Computer simulations with the MCY potential, *J. Chem. Phys.* 82 (1985) 5663.
- [16] I.G. Tironi, R. Sperb, P.E. Smith, W.F. van Gunsteren, A generalized reaction field method for molecular dynamics simulations, *J. Chem. Phys.* 102 (1995) 5451.
- [17] M. Praprotnik, D. Janezic, J. Mavri, Temperature dependence of water vibrational spectrum: a molecular dynamics simulation study, *J. Phys. Chem. A* 108 (2004) 11056.
- [18] H. Wang, Mathematical theory of molecular motors and a new approach for uncovering motor mechanism, *IEE Proc. Nanobiotechnol.* 150 (2003) 127–133.
- [19] F.M. Charron, M.G. Blanchard, J.Y. Lapointe, Intracellular hypertonicity is responsible for water flux associated with Na<sup>+</sup>/glucose cotransport, *Biophys. J.* 90 (2006) 3546–3554.
- [20] S. Nosé, A unified formulation of the constant temperature molecular dynamics method, *J. Chem. Phys.* 81 (1984) 511.
- [21] W.G. Hoover, Canonical dynamics: equilibrium phase-space distributions, *Phys. Rev. A* 31 (1985) 1695.
- [22] H. Rafii-Tabar, Modelling the nano-scale phenomena in condensed matter physics via computer-based numerical simulations, *Phys. Rep.* 325 (2000) 239–310.